Check for updates

ADVANCED QUANTUM TECHNOLOGIES
www.advquantumtech.com

Transfer Matrix Model for Emission Profile Optimization of Radial Gratings

Stefan Appel, Viviana Villafane, Jonathan J. Finley, and Kai Müller*

Radial Bragg gratings are commonly used to enhance light extraction from quantum emitters, but lack a well-suited, fast simulation method for optimization beyond periodic designs. To overcome this limitation, an algorithm based on the transfer matrix model (TMM) to calculate the free-space emission of such gratings is proposed and demonstrated. Using finite difference time domain (FDTD) simulations, free-space emission, and transfer matrices of single grating components are characterized. The TMM then combines any number of components to receive the total emission. Randomized benchmarks verify that results from this method agree within 98% with FDTD while reducing simulation time by one to two orders of magnitude. The speed advantage of this approach is shown by maximizing emission of a fifteen-trench circular grating into a Gaussian mode. It is expected that this novel algorithm will facilitate the optimization of radial gratings, enabling quantum light sources with unprecedented collection efficiencies.

1. Introduction

Radial symmetric structures such as radial Bragg gratings or Bullseye resonators are of great interest to enhance collection efficiency and emission rate of single quantum emitters. They are especially promising for spin-photon-interfaces and bi-frequency polarization-entangled photon pair sources, as they are insensitive to light polarization and provide Purcell enhancement over a wide spectral range.[1–3] Most designs thereby employ a periodic grating design.[1,2,4–9]

Transfer matrix models (TMMs) have been used for decades to predict the behavior of flat, stratified optical systems, such as distributed Bragg reflectors (DBRs), subject to plane wave illumination.[10–12] Already in the 1990s, TMMs were adapted for radially curved layers with impinging radial propagating waves.[13–15] This has also led to improved designs for radial DBRs, deviating from the strict periodicity of planar DBRs to compensate for effects only occurring in radial wave propagation.[15–18] In the non-curved case, it was also shown that non-periodic linear grating couplers can scatter light into a target mode more efficiently than periodic ones.[19–21]

Even though both the curved geometry and the results for linear waveguide couplers therefore suggest a non-periodic design for radial Bragg gratings, most publications today still revert to use a plane wave TMM and/or periodic radial structure.[1,2,4–9] The large computational cost of simulating any radial structure using the most common, rectangular, three-dimensional finite difference time domain (FDTD) method hinders the development of non-periodic radial geometries, and thus, their implementation in optical nanostructures. To make optimization feasible, a periodic design is preferred with a small number of free parameters. This reduces the number of design iterations needed for optimization, such that the total computational requirements remain manageable.

For an alternative simulation method, Li et al.[22] introduced the idea to use TMM to predict the field scattered into free-space from structures such as non-periodic gratings. Their 2D method is fast and shows excellent overlap with 2D FDTD simulation. Their TMM however is limited to non-curved, linear geometries and cannot predict the emission of a circular or radial grating. Since they aim at optimizing a radial grating, they therefore only use their TMM method to find a starting point for their structure. From this starting point, they drop the TMM approach and instead employ 3D FDTD combined with a gradient descent algorithm to find the optimal design for their radial grating.[22]

To overcome the computational hurdles associated with non-periodic radial grating designs and expand on the work of Li et al.[22] we present here a radial scatter-field TMM (rsTMM). In contrast to Li et.al, our rsTMM is capable of predicting the scattered field not for linear but for radial structures, and can deal with more than one guided modes in the substrate. The

S. Appel, K. Müller
Walter Schottky Institut
Department of Electrical and Computer Engineering
MCQST
Technische Universität München
85748 Garching, Germany
E-mail: stefan.appel@wsi.tum.de
V. Villafane, J. J. Finley
Walter Schottky Institut
Physics Department
School of Natural Sciences
MCQST
Technische Universität München
85748 Garching, Germany

The ORCID identification number(s) for the author(s) of this article can be found under https://doi.org/10.1002/qute.202300372

© 2024 The Authors. Advanced Quantum Technologies published by Wiley-VCH GmbH. This is an open access article under the terms of the Creative Commons Attribution-NonCommercial License, which permits use, distribution and reproduction in any medium, provided the original work is properly cited and is not used for commercial purposes.

DOI: 10.1002/qute.202300372

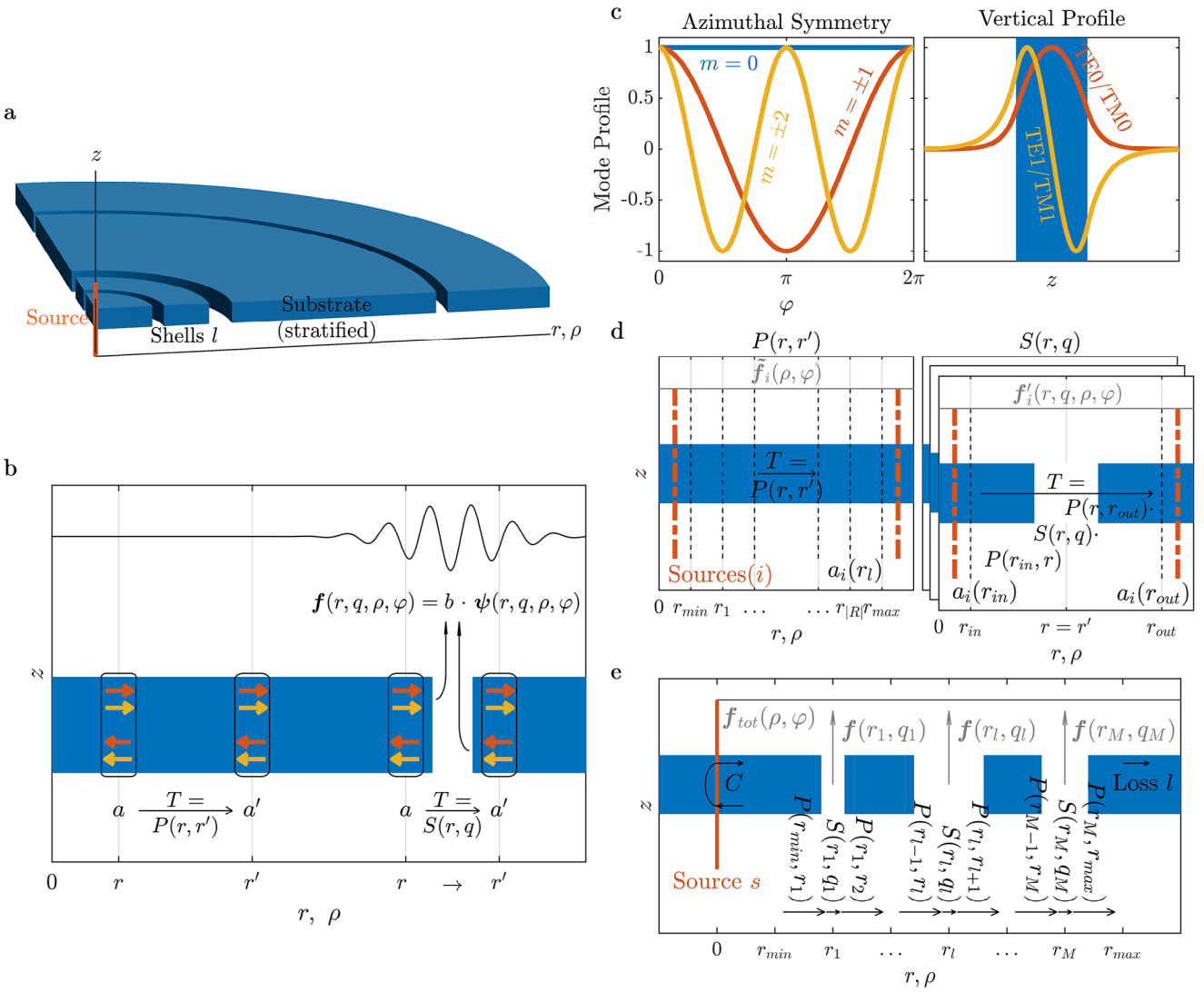

Figure 1. Concept of the the radial scatter transfer matrix model (rsTMM) a) Sketch of the structure to be simulated. A centered source is embedded into a (stratified) substrate, with concentric shells *l* of arbitrary scatterers surrounding it. b) Basic concept of the rsTMM. The substrate of interest supports modes (orange arrows), propagating inward or outward. The complex vectors *a*, *a*′ give the mode amplitudes at a fixed radius *r*, *r*′. Propagation (*P*, left), as well as scattering (*S*, right) between the modes is described by transfer matrices *T*. Emission into free-space from modes impinging on a scatterer is described by fields $\boldsymbol{f}$, which are calculated as linear combination scaled by the impinging mode amplitudes *b* (for details: see main text). c) The modes we consider are guided modes, characterized by the combination of their azimuthal symmetry (left) and their vertical profile (right) governed by the substrate. d) Transfer matrices are calculated from sets of simulations *i*, employing single mode sources at either the inner or outer position. The undisturbed substrate (left) yields all propagation transfer matrices *P*, a substrate with a single scatterer yields the scatterer transfer matrix *S* for this scatterer with geometry *q* at radius *r* (right). Simulations have to be repeated to form a database of different scatterers. e) The complete structure is assembled by multiplying the scatter *S* and propagation *P* transfer matrices, then applying boundary conditions for the source *s*, center reflection *C* and side-loss *l*. Finally, the coherent sum over the emission of all scatter shells gives the total free-space emission $\boldsymbol{f}_{\text{tot}}$.

performance of the rsTMM is confirmed by comparing results of simulations to 2D radial FDTD (rFDTD)[23] for various structures. Here, an error of less than 2% is achieved while saving a factor of 10 to 100 in computation time.

2. Method Definition

Our rsTMM aims to describe a structure as presented in **Figure 1a**. In a planar substrate with a centered source, *M* circular shells of scatterers are placed, where both the radius r_l and parameters or shape q_l of any scatter layer *l* may be changed independently within a set of allowed radii *R* and parameters *Q*. Such devices are commonly known as a Bullseye resonators, respectively as a circular, radial or cylindrical DBRs or gratings.[1,2,16,17,22] To explore the parameter space of the complete device, e.g., for optimization, the computational effort will scale unfavorably according to $|R|^M \cdot |Q|^M$. As such, we describe this system using a TMM instead and will demonstrate this approach to be quick in assembling any combination of scattering shells. Most of the computational effort is then only needed to characterize a single

© 2024 The Authors. Advanced Quantum Technologies published by Wiley-VCH GmbH

25119044, 2024, 4, Downloaded from https://onlinelibrary.wiley.com/doi/10.1002/qute.202300372, Wiley Online Library on [17/04/2024]. See the Terms and Conditions (https://onlinelibrary.wiley.com/terms-and-conditions) on Wiley Online Library for rules of use; OA articles are governed by the applicable Creative Commons License

shell in its 2D parameter space, a computation effort scaling as $|R| \cdot |Q|$. Our results show that when iterating through many different structures with many shell parameters to vary, our TMM method is faster than directly simulating the structures. Importantly, this approach is not only valid for radial structures as described here, but any kind of structure with many parts that can be separated in a TMM.

The basic concept of TMM is shown in Figure 1b. Individual scatterers (right), as well as mode propagation paths in the substrate (left) are expressed by transfer matrices T, which relate mode amplitudes a, a' at different radial positions $r < r'$, or on the inside and outside of a thin scatterer where $r \to r'$[24,25]

$$a' = T \cdot a \tag{1}$$

Both a and a' thereby are $2N$-dimensional vectors, where N is the total number of different modes j considered. One half of the entries for each vector represent outward (+) and the other half inward (−) traveling mode amplitudes. We determine T for any object by running a set of simulations i, recording a_i and a'_i for each. If there is a vector base for the mode amplitude space among a_i, then we can calculate T by representing the according amplitude vectors by matrices

$$A = \left[a_1 \dots a_i \dots a_{2N}\right], A' = \left[a'_1 \dots a'_i \dots a'_{2N}\right] \tag{2}$$

and inverting the transfer matrix Equation (1)

$$T = A' \cdot A^{-1} \tag{3}$$

where the existence of the matrix inverse A^{-1} is guaranteed by the vectors a_i spanning a complete basis. In practice, we find such a basis by running $2N$ simulations, where for every simulation i, we inject only one mode j, once on the inside and once on the outside of the object of interest as indicated in Figure 1d. As inward and outward propagation and scattering behavior is different due to the curved geometry,[13,14] one cannot assume symmetry to reduce the number of simulations by half (see Supporting Information, for further details on the simulation methods).

The modes we consider, as sketched in Figure 1c, are guided modes of the planar waveguide substrate at a single vacuum wavelength λ of the electro-magnetic field. Substrate examples may be single freestanding slabs or stratified dielectrics, possibly also including metals or dispersive media. All the following expressions depend on λ which we omit for clarity. Since we exclude non-linear effects, the vacuum wavelength will not change by propagation or scattering.

As the structure of interest is radially symmetric, each guided mode decomposes further into cylindrical modes with symmetry number m.[26] The symmetry number defines the azimuthal field dependence $\propto e^{im\varphi}$ with φ the azimuth angle. In total, we collect N individual propagating modes j each characterized by their vertical mode profile and their azimuth propagation symmetry.[26,27]

Since, we are only interested in electric dipole-like excitation and expect no scattering into modes having higher azimuthal symmetry indices due to the continuous radial symmetry of the structure, we can limit ourselves to $m = 0$ for vertical dipoles exciting E_z modes and $m = \pm 1$ for in-plane dipoles exciting H_z modes.[27] Furthermore, without loosing generality we can combine $m = \pm 1$ to a $\cos(\varphi)$ dependence to represent the symmetry of an in-plane dipole oriented along $\varphi = \pi/2$.[27] Note that structures with discrete radial symmetries may be simulated if modal symmetry m is not limited.

To describe the propagation of radial waves in the substrate between two radii r, r', we require the propagation transfer matrices $P(r, r')$. Figure 1d (left) shows how to obtain them: One set of simulations i is run without any scatterers present in the substrate, recording the mode amplitudes $a(r)$ at regular spacing. Following Equation (1), we then calculate propagation matrices between arbitrary positions

$$P(r, r') = A(r') \cdot A(r)^{-1} \tag{4}$$

Close to a source at $r = 0$, we receive non-zero inward propagating mode amplitudes due to the reactive near field known from antenna theory.[28] This effect does not appear in flat geometries, since the corresponding plane wave sources are infinitely extended. Also, we observe a non-linear phase evolution close to $r = 0$ due to the wavefront curvature. These propagation simulations are also used to detect undesired stray fields $\tilde{\boldsymbol{f}}'_i(\rho, \varphi)$ emitted by imperfect sources into free-space.

Similar, in order to describe a single scatter shell p at radius r, we compute a transfer matrix $S(r, p)$ by running a set of simulations with the respective shell as shown in Figure 1d (right). We record the mode amplitudes inside $a(r_{\text{in}})$ and outside $a(r_{\text{out}})$ of the shell, with $r_{\text{in}} < r < r_{\text{out}}$. The total transfer matrix T describing both the scatter as well as the propagation to and from it is then obtained from Equation (1):

$$\begin{aligned} T(r, q, r_{\text{out}}, r_{\text{in}}) &= A(r_{\text{out}}) \cdot A(r_{\text{in}})^{-1} \\ &= P(r, r_{\text{out}}) \cdot S(r, q) \cdot P(r_{\text{in}}, r) \end{aligned} \tag{5}$$

Left and right multiplying the inverse of the according propagation matrices P, we can then extract $S(r, q)$.

In addition, each shell may emit into free-space when a propagating mode is incident upon it as sketched in Figure 1b, such that the total emitted fields are given by the coherent sum of the fields emitted by all shells combined.[22] As the field emitted per shell is dependent on which mode was incident from which side, we represent it by a position- and parameter-dependent $2N$-element vector $\boldsymbol{\psi}(r, q, \rho, \varphi)$, with every entry $\boldsymbol{\psi}_{\pm j}(r, q, \rho, \varphi)$ representing all electric $\mathbf{E}$ and magnetic $\mathbf{H}$ field components. One half of the entries thereby give the fields emitted for a mode impinging from inside outward (+), the other for a mode impinging from outside inward (−). To recover these free-space fields, we employ the simulations i used to determine $S(r, q)$ before. As shown in Figure 1d, we record the field $\boldsymbol{f}'_i(r, q, \rho, \varphi)$ at a fixed distance z above the substrate.[22] For continuous rotational symmetric scatterers, the azimuthal symmetry will be the same as the symmetry of the impinging mode, such that the field may be restored from a record at a single azimuthal angle φ only. The previously determined stray fields are then subtracted from imperfect sources to end up with $\boldsymbol{f}_i(r, q, \rho, \varphi) = \boldsymbol{f}'_i(r, q, \rho, \varphi) - \tilde{\boldsymbol{f}}'_i(\rho, \varphi)$. However, the field retrieved in this way may still be created by a

© 2024 The Authors. Advanced Quantum Technologies published by Wiley-VCH GmbH

25119044, 2024, 4, Downloaded from https://onlinelibrary.wiley.com/doi/10.1002/qute.202300372, Wiley Online Library on [17/04/2024]. See the Terms and Conditions (https://onlinelibrary.wiley.com/terms-and-conditions) on Wiley Online Library for rules of use; OA articles are governed by the applicable Creative Commons License

multitude of modes impinging on the scatterer from inside and outside like sketched in Figure 1b, such that

$$\boldsymbol{f}_i(r, q, \rho, \varphi) = b_i \cdot \boldsymbol{\psi}(r, q, \rho, \varphi) \tag{6}$$

with b_i the impinging mode amplitude vector defined as

$$b_i = \left[a_i^+(r), a_i'^-(r)\right] \tag{7}$$

To obtain $\boldsymbol{\psi}(r, q, \rho, \varphi)$, we first calculate the mode amplitudes $a_i(r)$, $a_i'(r)$ on the inside respectively outside of the shell using the propagation matrices

$$\begin{aligned} a_i(r) &= P(r_{\text{in}}, r) a_i(r_{\text{in}}) \\ a_i'(r) &= P(r, r_{\text{out}})^{-1} a_i(r_{\text{out}}) \end{aligned} \tag{8}$$

to extract the impinging amplitudes b_i. Stacking the results from the set of simulations i to build a matrix B from b_i and a position-dependant vector $\boldsymbol{f}(\rho, \varphi)$ from $\boldsymbol{f}_i(\rho, \varphi)$, we can invert Equation (6) to calculate

$$\boldsymbol{\psi}(r, q, \rho, \varphi) = B^{-1} \cdot \boldsymbol{f}(r, q, \rho, \varphi) \tag{9}$$

By repeating this procedure for any number of different scatterers q at different radii r as indicated in Figure 1d, we build a look-up table for transfer matrices $S(r, q)$ and free-space fields $\boldsymbol{\psi}(r, q, \rho, \varphi)$. Linear interpolation allows us to also retrieve results in between the sampled radii.

Using both propagation- and scattering-type transfer matrices, we can now assemble any combination of scatterers at various positions into a multi-shell structure as sketched in Figure 1e. The according total transfer matrix T_{tot} is the product of the alternating scatter and propagation matrices

$$\begin{aligned} a(r_{\max}) &= T_{\text{tot}} \cdot a(r_{\min}) \\ &= P(r_M, r_{\max}) \cdot S(r_M, q_M) \cdot P(r_{M-1}, r_M) \cdots \\ &\quad P(r_1, r_2) \cdot S(r_1, q_1) \cdot P(r_{\min}, r_1) \cdot a(r_{\min}) \end{aligned} \tag{10}$$

The total transfer matrix therefore relates mode amplitudes on the inside $a(r_{\min})$ and outside $a(r_{\max})$ of the structure. To fix the actual mode amplitudes, we employ open or impedance-matched boundary conditions on the outside

$$a_j^+(r_{\max}) = l_j \qquad a_j^-(r_{\max}) = 0 \tag{11}$$

with the per-mode side losses l_j remaining as free parameters.

On the inside, we inject only outward propagating modes representing the source, initially with zero reflection:

$$\tilde{a}_j^+(r_{\min}) = s_j \qquad \tilde{a}_j^-(r_{\min}) = 0 \tag{12}$$

The complex source amplitudes s_j may be determined by another simulation recording mode amplitudes at $r_{\min}$ with only the desired source present. Note that a multi-mode source may be used, however, the amplitude ratio between the modes may be changed by Purcell effect that will be addressed in future work.

So far, we have not addressed inward reflections from the structure, and the boundary conditions $\tilde{a}(r_{\min})$, $a(r_{\max})$ cannot be satisfied except for the trivial, scatter-free case. To account for reflections, we have to consider that any reflected, inward propagating mode amplitude, at the center $r = 0$, will change into an outward propagating mode amplitude, which then is subject to reflections again. Therefore, we sum up all infinite reflections in a Neumann series and end up with an inner boundary condition

$$a(r_{\min}) = \sum_{n=0}^{\infty} C^n \cdot \tilde{a}(r_{\min}) = (I - C)^{-1} \cdot \tilde{a}(r_{\min}) \tag{13}$$

with the identity I and the center reflection matrix C

$$\begin{aligned} C_{j+,k+} &= 0, \qquad C_{j+,k-} = \delta_{j,k}\varphi_j, \qquad C_{j-,k-} = 0 \\ C_{j-,k+} &= -\sum_{l=0}^{N} \left(\Theta_{\text{tot}}^{-1}\right)_{j-,l-} \cdot \left(T_{\text{tot}}\right)_{l-,k+} \end{aligned} \tag{14}$$

$C_{j-,k+}$ describes the reflection of outward-traveling mode $k+$ into inward-traveling mode $j-$ by the structure with $\Theta_{\text{tot}} = ((T_{\text{tot}})_{-j,-k})$ a $N \times N$ sub-matrix of the transfer matrix T_{tot}. $C_{j+,k-}$ is the transmission through the center with some phase shift φ_j depending on the mode j, which would vanish $\varphi_j \to 1$ for $r_{\min} \to 0$. We determine the phase shift as $\varphi_j = a_j^+(r_{\min})/a_j^-(r_{\min})$ using one of the previous simulations with mode injection from the outside.

Now that we have taken care of all reflections, the boundary conditions can be fulfilled and we solve for the side-losses l_j using Equation (10).

Finally, we can now calculate the scattered free-space field of the structure. For this, we first calculate the mode amplitudes inside ($a(r_i)$) and outside ($a'(r_i)$) of all scattering shells i by successively applying Equation (1), alternating between P and S matrices and starting from the injected amplitudes $a(r_{\min})$. Using Equation (7), we can then retrieve the impinging amplitudes $b(r_i)$ and from there calculate the emitted fields $\boldsymbol{f}(r_i, p_i, \rho)$ for every shell by Equation (6). Coherently adding up all fields, we obtain the total free-space field

$$\boldsymbol{f}_{tot}(\rho, \varphi) = \sum_{i=1}^{M} \boldsymbol{f}(r_i, q_i, \rho, \varphi) \tag{15}$$

3. Benchmark Results and Discussion

To verify our such-defined rsTMM, we simulate a benchmark system and compare the results to established rFDTD.[23] The benchmark substrate consists of a freestanding, dielectric diamond membrane with refractive index of 2.4114 and thickness of 140nm, surrounded by air. It is fully penetrated by rectangular cross-section trenches of varying width and radii. The wavelength of interest is 620nm, leading to one guided E_z and H_z mode each, with effective refractive indices of 1.551 and 2.023, respectively. Radial symmetry is limited to $m = 0$ ($m = 1$) for the E_z (H_z) mode. For all benchmark situations, centered E_z and H_z sources, coupling to the respective modes, are simulated separately. We record the free-space field at a distance of z =620nm

© 2024 The Authors. Advanced Quantum Technologies published by Wiley-VCH GmbH

25119044, 2024, 4, Downloaded from https://onlinelibrary.wiley.com/doi/10.1002/qute.202300372, Wiley Online Library on [17/04/2024]. See the Terms and Conditions (https://onlinelibrary.wiley.com/terms-and-conditions) on Wiley Online Library for rules of use; OA articles are governed by the applicable Creative Commons License

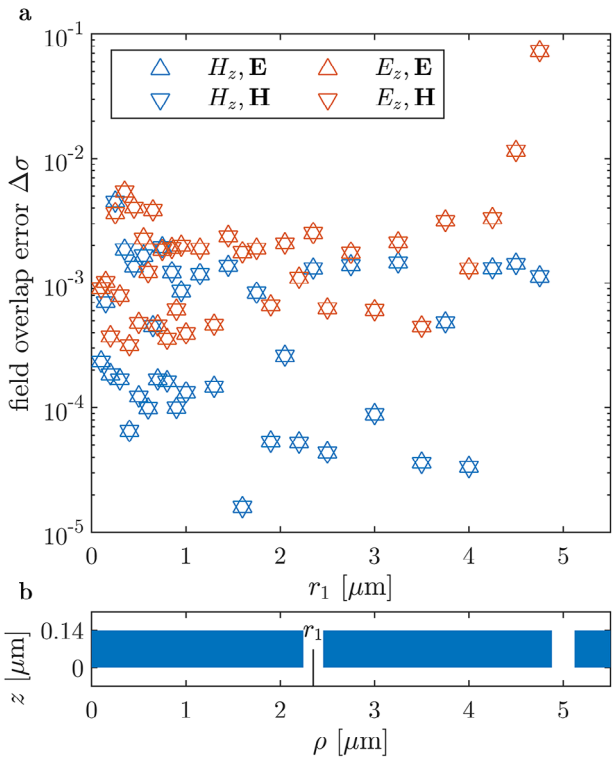

Figure 2. Benchmark of rsTMM for varying radii r_1. a) Error in field overlap $\Delta\sigma$ for **E** and **H** fields between rsTMM and rFDTD for a centered E_z or H_z mode source. b) Example for one of the benchmark structures. The inner trench radius r_1 is varied while choosing random trench widths.

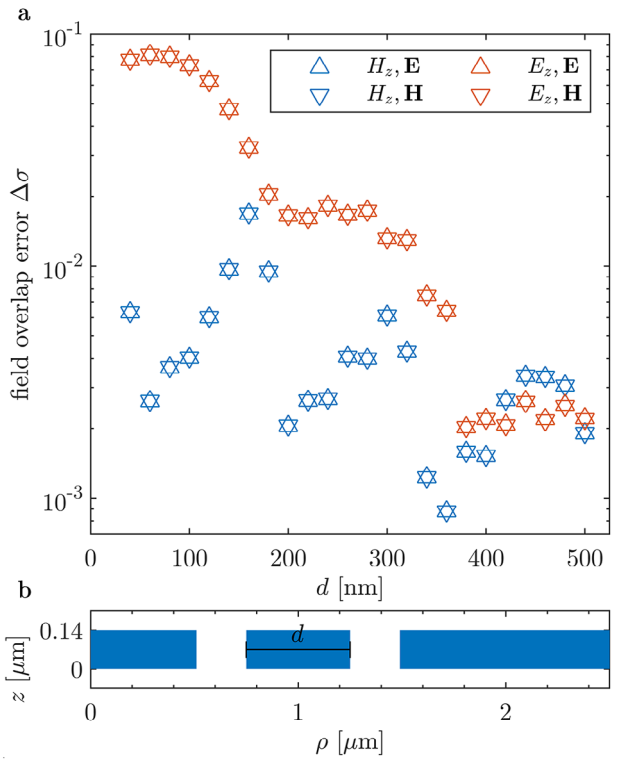

Figure 3. Benchmark of rsTMM for varying trench distances d. a) Error in field overlap $\Delta\sigma$ for **E** and **H** fields between rsTMM and rFDTD for a centered E_z or H_z mode source. b) Example for one of the benchmark structures. The trench distance d is varied with the trench widths fixed.

above the membrane, and compare it to the results by rFDTD using the normalized squared field overlap[22]

$$\sigma(f_{\mathrm{rsTMM}}, f_{\mathrm{rFDTD}}) = \frac{\left|\iint f_{\mathrm{rsTMM}}(\rho,\phi)\circ f^{*}_{\mathrm{rFDTD}}(\rho,\phi)\rho \mathrm{d}\varphi \mathrm{d}\rho\right|^2}{\iint \left|f_{\mathrm{rsTMM}}(\rho,\phi)\right|^2 \rho \mathrm{d}\varphi \mathrm{d}\rho \cdot \iint \left|f_{\mathrm{rFDTD}}(\rho,\phi)\right|^2 \rho \mathrm{d}\varphi \mathrm{d}\rho} \tag{16}$$

For similar results, the overlap should tend toward 1, such that we focus on the difference or error $\Delta\sigma = 1 - \sigma$. We separately investigate both the electric $f =: \mathbf{E}$ and magnetic $f =: \mathbf{H}$ fields.

For the first benchmark series, we place two trenches as sketched in **Figure** 2b. The inner trench radius is varied continuously while choosing random trench widths, while the outer trench radius is fixed and the trench width is optimized for maximum mode reflection. Using this arrangement, we can test the amplitude and phase relation between free-space fields created by inner versus outer trench, as well as inward versus outward mode impingement. The error in the field overlap for this series is presented in Figure 2a, with blue (orange) triangles showing the case for an excitation with the H_z (E_z) mode. Upward (downward) pointing triangles show the error in the **E** (**H**) field, respectively.

Importantly, for the data plotted in Figure 2a the average simulation time was 0.60 ± 0.03 s for rsTMM and 100 ± 85s for rFDTD, i.e., the rsTMM simulations were more than a factor of 100 faster. For most radii, we find an error of below 1% between standard computation techniques and the approach presented in this manuscript. In general, the H_z mode agrees better than the E_z mode. For large radii of the inner trench, especially the E_z mode shows larger errors. We suspect that this does not stem from the large trench radius but rather from the small distance between the two trenches.

To investigate this effect with a second benchmark, we place two wide trenches around 1 μm radius at varying distance to each other as sketched in **Figure** 3b. We choose wide trenches to maximize emission into free-space, as we think the effect may be caused by absorption of free-space modes by the neighboring trench. We do not cover this free-space coupling path with our rsTMM, as we do not include absorption from free-space. As free-space modes should propagate away with distance, we expect a recovery in field overlap with increasing trench distance. The corresponding error in field overlap for varying trench distances is shown in Figure 3a, again with blue (orange) triangles representing excitation with the H_z (E_z) mode and upward (downward) pointing triangles relating to errors in the **E** (**H**) field.

As expected, both modes show increased errors up to 10% for trenches placed at small distances, but recover below 1% for larger distances. Superimposed, we observe a beating in the error, which we attribute to resonances in the combined free-space and guided mode coupling. For sufficiently large radial spacing between scattering elements, our rsTMM method therefore only deviates within 1% from the established rFDTD method. Similar to before, the rsTMM simulations were much faster with

© 2024 The Authors. Advanced Quantum Technologies published by Wiley-VCH GmbH

25119044, 2024, 4, Downloaded from https://onlinelibrary.wiley.com/doi/10.1002/qute.202300372, Wiley Online Library on [17/04/2024]. See the Terms and Conditions (https://onlinelibrary.wiley.com/terms-and-conditions) on Wiley Online Library for rules of use; OA articles are governed by the applicable Creative Commons License

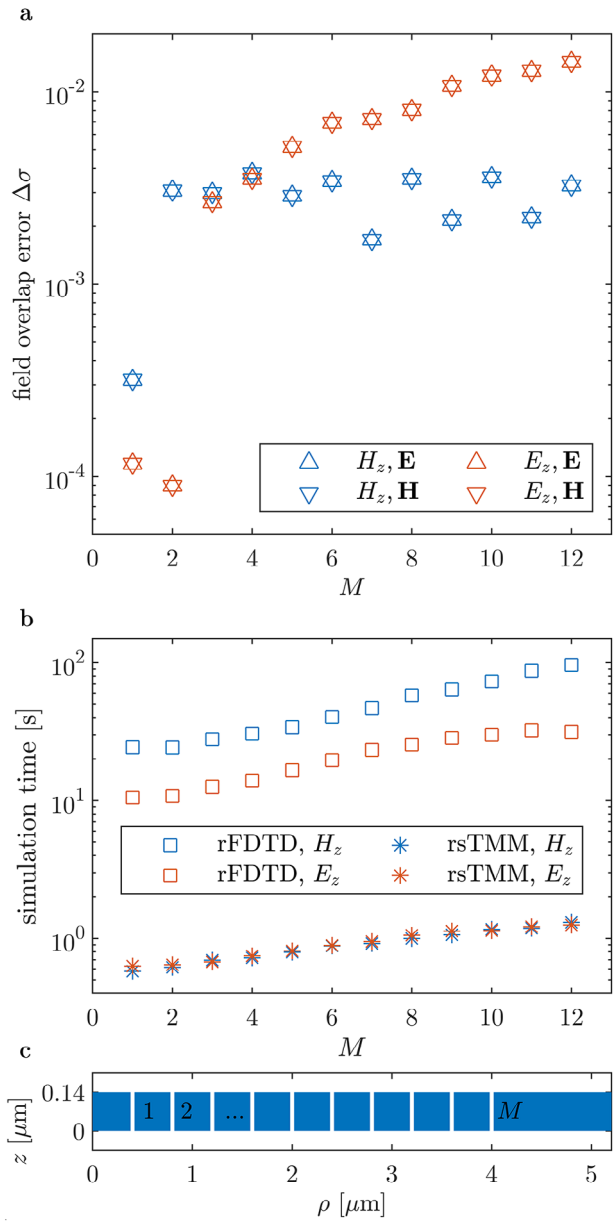

Figure 4. Benchmark of rsTMM for varying trench number M. a) Error in field overlap $\Delta\sigma$ for **E** and **H** fields between rsTMM and rFDTD for a centered E_z or H_z mode source. b) Simulation time required to run the benchmark with rFDTD or rsTMM, for both sources, respectively. c) Example for one of the benchmark structures. The number of trenches M is varied with trench widths and distances fixed.

simulation times per data point of 0.60 ± 0.03 s for rsTMM and 21 ± 10 s for rFDTD.

For a final benchmark, we investigate the scaling of computation time and error with increasing number of scattering shells. Thin trenches are chosen to minimize the emission and reflection per trench, such that the contribution of each trench to the total free-space field is comparable. As sketched in **Figure** 4c, the trenches are placed at a distance of 400nm to each other, in order to minimize the free-space coupling effect, and are added from the center outward. The error and time requirements are shown in Figure 4a,b, respectively. The color scheme follows the previous figures, with blue (orange) representing the excitation with the H_z (E_z) mode.

For an increasing number of scatterers, the error between rsTMM and rFDTD levels off for the H_z-mode but keeps increasing for the E_z-mode, both for the **E** fields (upward triangles) and **H** fields (downward triangles). We attribute this to the generally higher error rate in previous benchmarks for the E_z mode. With an initially higher error for two trenches, the combined error will scale worse with increasing trench number. Importantly, the error still remains within the single-digit percent range.

The time for rsTMM (star symbols in Figure 4b) grows approximately linear with the number of trenches, but stays within the few-second regime. We therefore assume that most time in our rsTMM method is spent on interpolations from the scatterer look-up table and possibly on matrix multiplications, while the contribution from the matrix inversion to solve the boundary conditions is small. In contrast, rFDTD simulations on the same machine (open squares in Figure 4b) take between a factor of 10 to 100 longer. The growth law cannot be clearly identified here, but data suggests a significant minimum time requirement. As rFDTD simulations function by propagating fields time step by time step until most of the energy has been emitted from the structure, any extra scatterer reflecting back to the center additionally increases the simulation time.

4. Optimization Results and Discussion

With rsTMM established as much faster but possibly less exact than rFDTD simulations, we now aim to showcase the speed advantage for simulating a large number of structures including lots of scatter shells. To this end, we optimize a Bullseye resonator with $M = 15$ fully etched trenches for maximal emission rate from a single mode source centered in the slab into a Gaussian mode, similar as described by Li et al.[22] The numerical aperture of the target mode is fixed to $NA = 0.4$ and both radius r_i and width w_i of each trench are varied individually. In order to account for fabrication constraints in future experimental realizations, the minimum feature size is set to 50nm and the maximum radius r_M is set to 5 µm. Trench distances $\Delta r_i = r_{i+1} - r_i$ are varied between 150 and 450 nm, and the trench widths are limited to < 240 nm.

Our figure of merit is the power emitted upward into the target Gaussian mode:

$$FOM = \frac{\mathfrak{Re}\left[\xi_{\text{Target,rsTMM}} \cdot \xi_{\text{rsTMM,Target}}\right] \cdot \Gamma_{\text{Top}}}{\left|\xi_{\text{Target,Target}}\right| \cdot \left|\xi_{\text{rsTMM,rsTMM}}\right|} \tag{17}$$

with the overlap integral

$$\xi_{i,j} = \iint \mathbf{E}_i(\rho,\phi) \times \mathbf{H}_j^*(\rho,\phi) \circ \hat{z}\, \rho\, \mathrm{d}\varphi \mathrm{d}\rho \tag{18}$$

and the upward emission ratio

$$\Gamma_{\text{Top}} = 0.5 \cdot \left(1 - \frac{\sum_j |a_j^+(r_{\min})|^2}{\sum_j |I_j|^2}\right) \tag{19}$$

© 2024 The Authors. Advanced Quantum Technologies published by Wiley-VCH GmbH

25119044, 2024, 4, Downloaded from https://onlinelibrary.wiley.com/doi/10.1002/qute.202300372, Wiley Online Library on [17/04/2024]. See the Terms and Conditions (https://onlinelibrary.wiley.com/terms-and-conditions) on Wiley Online Library for rules of use; OA articles are governed by the applicable Creative Commons License

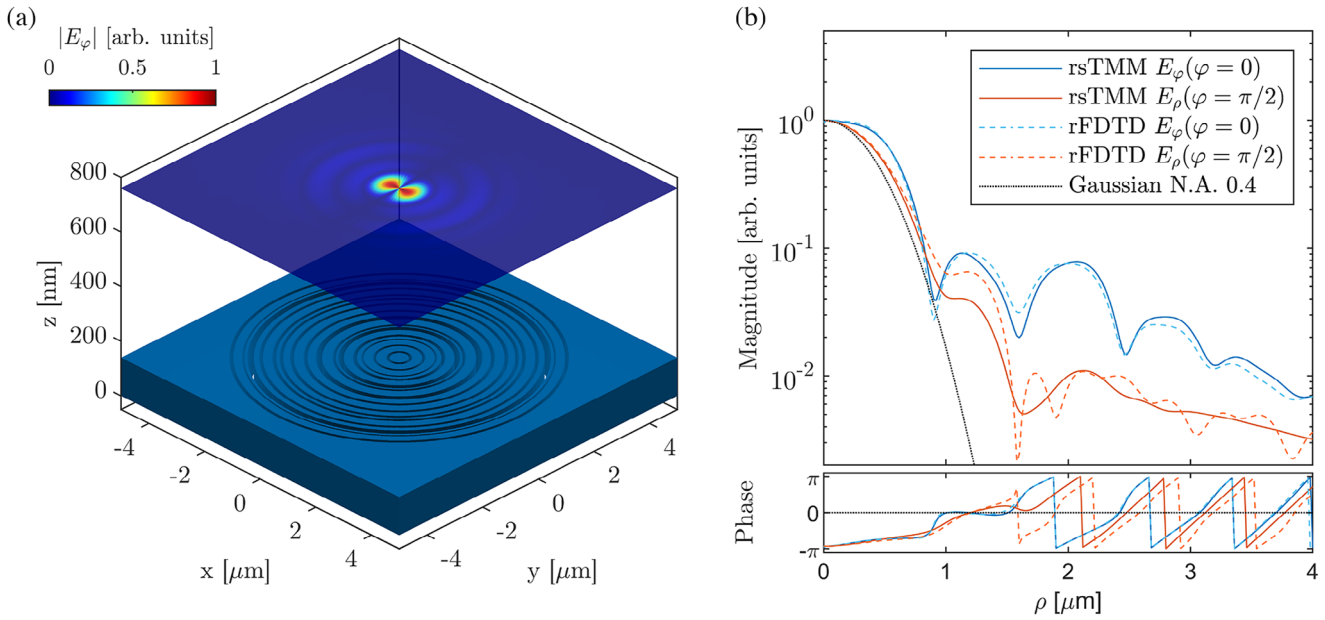

Figure 5. a Emission profile (top) achieved with a) bullseye structure (bottom), as optimized and simulated using rsTMM. b) Radial field profiles comparing results from rsTMM and rFDTD against the target Gaussian mode. The emission into the targeted Gaussian with *N.A.* = 0.4 is 42.44%, the overlap between rFDTD and rsTMM 98%.

The fraction thereby gives the ratio of power lost through the side, and the pre-factor of 0.5 accounts for the z mirror symmetry, leading to equal top and bottom emission. For the optimization, we use a surrogate algorithm delivered with MATLAB. After simulating 2896 different structures within 1.75h we achieve 42.44% top emission into the target Gaussian mode, of 50% theoretically possible. The corresponding, optimized structure and its emitted E_φ-field are shown in **Figure 5**a. Interestingly, the optimized structure (Figure 5a bottom) shows no sign of radial periodicity. To verify our optimization result, we again compare the field profile obtained using rsTMM and rFDTD simulation. Field profile cuts are plotted in Figure 5b as solid (rsTMM) and dashed (rFDTD) lines, along the x-axis ($\varphi = 0$) for the E_φ component (blue) and along the y-axis ($\varphi = \pi$) for the E_ρ component (orange). The absolute error between the curves is small; only on the logarithmic scale the relative errors at small field amplitudes become visible. We calculate the error in field overlap between rFDTD and rsTMM to quantify the deviation and find $\Delta\sigma$ =2% both for **E** and **H** fields. The small increase in error compared to the previous benchmarks results from combining more scattering shells at closer distances.

Finally, we take a look at the time requirements of the two different methods. The simulation time for the final structure was 1.5s for rsTMM and 180s for rFDTD on the same machine. Assuming a constant simulation time throughout the optimization, we find that the 1.75h total simulation time contains an overhead of 0.5h from the optimization algorithm. Strikingly, if we had used rFDTD simulations for the optimization, the estimated total optimization time would therefore have been 145h, again assuming a constant simulation time for each structure. For a fair comparison, the time required to create the look-up tables for the scatterers has to be considered as well, which for this benchmark was 63h. This means that even in the worst case, more than 80h of simulation time was saved for one optimization run. However, since the look-up table can be re-used for any further optimization using the same set of scatterers and the same substrate, the time advantage per actual use case is significantly higher.

5. Conclusion

To summarize, we have introduced a new simulation method for radial symmetric scattering shell structures in planar substrates supporting few guided modes. Our rsTMM agrees within 98% with established rFDTD methods except for free-space coupling effects occurring for closely spaced scattering shells. The method is up to 100 times faster than rFDTD, allowing for fast structure optimization in large parameter spaces. We expect that our novel simulation technique will lead to the implementation of more non-periodic and curved nano-photonic grating structures, and may grant access to new collection efficiency records for photonic quantum emitters.

Supporting Information

Supporting Information is available from the Wiley Online Library or from the author.

Acknowledgements

The authors gratefully acknowledged financial support from the German Federal Ministry of Education and Research via the funding program Photonics Research Germany (project MOQUA (13N14846)), the European Union's Horizon 2020 research and innovation program under Grants Agreement No. 862035 (QLUSTER), the Deutsche Forschungsgemeinschaft (DFG, German Research Foundation) via the projects PQET (INST

© 2024 The Authors. Advanced Quantum Technologies published by Wiley-VCH GmbH

25119044, 2024, 4, Downloaded from https://onlinelibrary.wiley.com/doi/10.1002/qute.202300372, Wiley Online Library on [17/04/2024]. See the Terms and Conditions (https://onlinelibrary.wiley.com/terms-and-conditions) on Wiley Online Library for rules of use; OA articles are governed by the applicable Creative Commons License

95/1654-1), MQCL (INST 95/1720-1) and CNLG (MU 4215/4-1), and Germany's Excellence Strategy (MCQST, EXC-2111, 390814868) and the Bavarian State Ministry of Science and Arts via the project EQAP.

Open access funding enabled and organized by Projekt DEAL.

Conflict of Interest

The authors declare no conflict of interest.

Data Availability Statement

The data that support the findings of this study are available from the corresponding author upon reasonable request.

Keywords

bullseye, collection efficiency, emission profile, radial bragg grating, transfer matrix model

Received: October 20, 2023
Revised: December 21, 2023
Published online: January 22, 2024

[1] M. Davanço, M. T. Rakher, D. Schuh, A. Badolato, K. Srinivasan, *Appl. Phys. Lett.* **2011**, *99*, 041102.
[2] L. Li, E. H. Chen, J. Zheng, S. L. Mouradian, F. Dolde, T. Schröder, S. Karaveli, M. L. Markham, D. J. Twitchen, D. Englund, *Nano Lett.* **2015**, *15*, 1493.
[3] H. Wang, Y.-M. He, T.-H. Chung, H. Hu, Y. Yu, S. Chen, X. Ding, M.-C. Chen, J. Qin, X. Yang, R.-Z. Liu, Z.-C. Duan, J.-P. Li, S. Gerhardt, K. Winkler, J. Jurkat, L.-J. Wang, N. Gregersen, Y.-H. Huo, Q. Dai, S. Yu, S. Höfling, C.-Y. Lu, J.-W. Pan, *Nat. Photonics* **2019**, *13*, 770.
[4] S. Ates, L. Sapienza, M. Davanço, A. Badolato, K. Srinivasan, *IEEE J. Sel. Top. Quantum Electron.* **2012**, *18*, 1711.
[5] K. Winkler, N. Gregersen, T. Häyrynen, B. Bradel, A. Schade, M. Emmerling, M. Kamp, S. Höfling, C. Schneider, *Phys. Rev. Mater.* **2018**, *2*, 052201.
[6] B. Yao, R. R. Su, Y. Y. Wei, Z. Liu, T. Zhao, J. Liu, *J. Korean Phys. Soc.* **2018**, *73*, 1502.
[7] N. M. H. Duong, Z.-Q. Q. Xu, M. Kianinia, R. Su, Z. Liu, S. Kim, C. Bradac, T. T. Tran, Y. Wan, L.-J. J. Li, A. Solntsev, J. Liu, I. Aharonovich, *ACS Photonics* **2018**, *5*, 3950.
[8] L. Rickert, T. Kupko, S. Rodt, S. Reitzenstein, T. Heindel, *Opt. Express* **2019**, *27*, 36824.
[9] S. Kolatschek, S. Hepp, M. Sartison, M. Jetter, P. Michler, S. L. Portalupi, *J. Appl. Phys.* **2019**, *125*, 045701.
[10] W. Weinstein, *J. Opt. Soc. Am.* **1947**, *37*, 576.
[11] L. I. Epstein, *J. Opt. Soc. Am.* **1952**, *42*, 806.
[12] F. Abelès, *J. Opt. Soc. Am.* **1957**, *47*, 473.
[13] Y. Jiang, J. Hacker, *Appl. Opt.* **1994**, *33*, 7431.
[14] E. Ping, *J. Appl. Phys.* **1994**, *76*, 7188.
[15] M. A. Kaliteevskiĭ, R. A. Abram, V. V. Nikolaev, G. S. Sokolovskii, *J. Mod. Opt.* **1999**, *46*, 875.
[16] D. Ochoa, R. Houdré, M. Ilegems, H. Benisty, *Phys. Rev. B - Condens. Matter Mater. Phys.* **2000**, *61*, 4806.
[17] M. E. Tobar, J. G. Hartnett, J. M. L. Floch, D. Cros, *Proc. IEEE Intl. Freq. Cont. Symp. Expo.* **2005**, *52*, 257.
[18] E. Ben-Bassat, J. Scheuer, *Opt. Lett.* **2015**, *40*, 3069.
[19] D. Taillaert, F. Van Laere, M. Ayre, W. Bogaerts, D. Van Thourhout, P. Bienstman, R. Baets, *Jpn. J. Appl. Phys.* **2006**, *45*, 6071.
[20] J. Lu, C. Petre, E. Yablonovitch, J. Conway, *J. Opt. Soc. Am. B* **2007**, *24*, 2268.
[21] C. Zhang, J.-H. Sun, X. Xiao, W.-M. Sun, X.-J. Zhang, T. Chu, J.-Z. Yu, Y.-D. Yu, *Chin. Phys. Lett.* **2013**, *30*, 014207.
[22] L. Li, H. Choi, M. Heuck, D. Englund, *Opt. Express* **2021**, *29*, 16469.
[23] A. F. Oskooi, D. Roundy, M. Ibanescu, P. Bermel, J. D. Joannopoulos, S. G. Johnson, *Comput. Phys. Commun.* **2010**, *181*, 687.
[24] C. Seguinot, P. Kennis, J.-F. Legier, F. Huret, E. Paleczny, L. Hayden, *IEEE Trans. Microwave Theory Tech.* **1998**, *46*, 536.
[25] M. J. Schmid, M. S. Müller, *Opt. Express* **2015**, *23*, 8087.
[26] A. C. Ludwig, *Comput. Phys. Commun.* **1991**, *68*, 306.
[27] C.-M. Tang, *IEEE Trans. Antennas Propag.* **1979**, *27*, 665.
[28] B. Derat, G. F. Hamberger, F. Michaelsen, *IET Microwaves, Antennas Propag.* **2019**, *13*, 2584.

© 2024 The Authors. Advanced Quantum Technologies published by Wiley-VCH GmbH

25119044, 2024, 4, Downloaded from https://onlinelibrary.wiley.com/doi/10.1002/qute.202300372, Wiley Online Library on [17/04/2024]. See the Terms and Conditions (https://onlinelibrary.wiley.com/terms-and-conditions) on Wiley Online Library for rules of use; OA articles are governed by the applicable Creative Commons License